Journal of Computational Physics 228 (2009) 3742–3761

Contents lists available at ScienceDirect

Journal of Computational Physics

journal homepage: www.elsevier.com/locate/jcp

A three-dimensional electrostatic particle-in-cell methodology on unstructured Delaunay–Voronoi grids

Nikolaos A. Gatsonis *, Anton Spirkin

Mechanical Engineering Department, Worcester Polytechnic Institute, 100 Institute Road, Worcester, MA 01609, USA

ARTICLE INFO

Article history:
Received 20 March 2008
Received in revised form 30 January 2009
Accepted 3 February 2009
Available online 12 February 2009

Keywords:
Three-dimensional particle-in-cell (PIC)
Unstructured PIC
Delaunay–Voronoi

ABSTRACT

The mathematical formulation and computational implementation of a three-dimensional particle-in-cell methodology on unstructured Delaunay–Voronoi tetrahedral grids is presented. The method allows simulation of plasmas in complex domains and incorporates the duality of the Delaunay–Voronoi in all aspects of the particle-in-cell cycle. Charge assignment and field interpolation weighting schemes of zero- and first-order are formulated based on the theory of long-range constraints. Electric potential and fields are derived from a finite-volume formulation of Gauss' law using the Voronoi–Delaunay dual. Boundary conditions and the algorithms for injection, particle loading, particle motion, and particle tracking are implemented for unstructured Delaunay grids. Error and sensitivity analysis examines the effects of particles/cell, grid scaling, and timestep on the numerical heating, the slowing-down time, and the deflection times. The problem of current collection by cylindrical Langmuir probes in collisionless plasmas is used for validation. Numerical results compare favorably with previous numerical and analytical solutions for a wide range of probe radius to Debye length ratios, probe potentials, and electron to ion temperature ratios. The versatility of the methodology is demonstrated with the simulation of a complex plasma microsensor, a directional micro-retarding potential analyzer that includes a low transparency micro-grid.

1. Introduction

This work is motivated by the need to model bounded plasmas, plasma microdevices and plasma sensors with complex geometries and boundary conditions. This work is directed towards the simulation of collisionless plasmas, described theoretically by the electrostatic Vlasov–Maxwell system of equations. This work establishes and validates a novel 3d, electrostatic, particle-in-cell (PIC) methodology on unstructured Voronoi–Delaunay grids (UPIC3dE).

Various implementations of electrostatic and electromagnetic PIC methods have been developed on three-dimensional structured and mostly uniform grids [1–3]. A structured grid allows for an easy implementation of numerical algorithms essential to PIC, such as high-order weighting, fast particle movers and tracers, and fast field solvers. Domain decomposition of the structured grid is also straightforward which is important in the design of the parallel PIC codes [4–7].

There are few implementations of PIC on unstructured grids. In 2d, Jacobs and Hesthaven [8] used unstructured triangular grids to implement an electrostatic PIC approach, while Sonnendrücker et al. [9] implemented a Darwin model on triangular finite-elements. A three-dimensional electromagnetic PIC method on non-uniform hexahedral grids was developed by Wang et al. [10,11]. The method is parallelized and takes advantage of the hexahedral cells that are connected with cubic cells, distorted to fit the complex geometries. Each hexahedral is mapped one to one to a unit cube in the logical Cartesian space. The

* Corresponding author.
E-mail address: gatsonis@wpi.edu (N.A. Gatsonis).

0021-9991/$ - see front matter © 2009 Elsevier Inc. All rights reserved.
doi:10.1016/j.jcp.2009.02.003

gather/scatter procedures are performed in the Cartesian space using a charge conserving weighting scheme by Villasenor and Buneman [12]. Wu et al. [13] developed a finite-element parallelized electrostatic code using 3d unstructured tetrahedral meshes with dynamic domain decomposition. Petillo et al. [14] developed a finite-element based code that includes both structured and unstructured grid systems.

While unstructured grids offer advantages in simulating bounded plasmas or plasma devices with complex geometries, they present challenges that relate with most aspects of the standard PIC cycle. In this paper we present the major mathematical and algorithmic contributions that establish a novel PIC formulation on unstructured 3d Delaunay–Voronoi grids (UPIC3dE). The new developments involve the unstructured grid generation, particle loading, particle injection, charge assignment, force interpolation, particle tracing and moving, and field solver. In Spirkin and Gatsonis [15] we presented initial results from UPIC3dE. The major conceptual contribution in our work is the use of the Delaunay–Voronoi in all aspects of the UPIC3dE cycle. Particle weight and force interpolation schemes are derived for Delaunay tetrahedra from the long-range constraints theory established by Hockney and Eastwood [2] for 2d Cartesian cells. The nodal values of charge density are derived using the Delaunay–Voronoi dual. The evaluation of the potential and electric field is obtained through a finite-volume method that discretizes Gauss' integral law using the Delaunay–Voronoi dual. Hermeline [16] utilized a similar approach for the numerical solution of the 2d Maxwell equations. Dirichlet and Neumann boundary conditions are implemented through Gauss's law. In addition, floating boundary conditions are developed for 3d unstructured Delaunay grids, following the 2d cartesian concept of Vahedi and DiPeso [17]. An improved particle-search algorithm is developed based on ideas found in [18] and aids to the numerical integration of the particle equations of motion. Error analysis and sensitivity follows the 2d3V formulation by Hockney [19] which is expanded to cover the 3d3V UPIC3dE methodology. The effects of particles/cell, grid scaling, and time-step on numerical heating, slowing-down time, and deflection times are evaluated in a parametric investigation. The UPIC3dE method is validated with as series of computations that compare numerical with theoretical and previous computational results of current collection by cylindrical probes in stationary and moving plasmas. Finally, in this paper the application of the UPIC3dE to the simulation of a micro-retarding potential analyzer extends considerably the preliminary results appeared in [15]. The UPIC3dE numerical results are compared with analytic solutions and demonstrate the three-dimensional geometric and space-charge effects not captured in the theory. The UPIC3dE methodology therefore, shows its applicability in the design of complex plasma devices and sensors.

In Section 2 the Vlasov–Poisson mathematical description of a collisionless plasma is summarized. The mathematical and numerical aspects of the UPIC3dE methodology are presented in Section 3. Error analysis and the evaluation of heating, slowing-down and deflection times are presented in Section 4. The validation of the code is discussed in Section 5. An implementation of UPIC3dE to the simulation of a plasma sensor with a complex geometry and boundary conditions, the directional micro-retarding analyzer, are presented in Section 6.

2. Mathematical description of collisionless electrostatic plasma

We consider a fully ionized plasma occupying a volume V consisting of several species denoted by the species index s each with N_s particles. A mathematical description of a collisionless plasma involves the electrostatic Vlasov–Maxwell system [20,21]. The single-particle distribution function for species s particles, gives the average number of particles in a volume $d^3r\,d^3v \equiv d\mathbf{r}\,d\mathbf{v}$ of the phase-space centered at a point $(\mathbf{r},\mathbf{v})$ as

$$f_s(\mathbf{r},\mathbf{v},t)d^3r\,d^3v = d^6N_s(t). \tag{1}$$

The local number density is then

$$n_s(r,t) = \int f_s(\mathbf{r},\mathbf{v},t)d^3v. \tag{2}$$

The equation for the distribution function is

$$\frac{\partial f_s}{\partial t} + \mathbf{v}\cdot\frac{\partial f_s}{\partial \mathbf{r}} + \frac{q_s}{m_s}[\mathbf{E}(\mathbf{r},t) + \mathbf{v}\times\mathbf{B}_{\text{ext}}(\mathbf{r},t)]\cdot\frac{\partial f_s}{\partial \mathbf{v}} = 0. \tag{3}$$

The electrostatic formulation assumes that there are no induced magnetic fields due to the particle motion. The self-consistent electric field (and potential) is due to the smoothed distribution (internal) ρ_{int} and external distribution of charges ρ_{ext}, and is given by Maxwell's equations that reduce to the integral Gauss's law

$$\oint\!\!\!\oint_S \mathbf{E}\cdot d\mathbf{S} = \frac{1}{\varepsilon_o}\int\int\int_V \rho\, dV \tag{4}$$

or to the differential Poisson's equation

$$\varepsilon_0\nabla\cdot\mathbf{E}(\mathbf{r},t) = \varepsilon_0\nabla\cdot(\mathbf{E}_{\text{ext}}(\mathbf{r},t) + \mathbf{E}_{\text{int}}(\mathbf{r},t)) = \sum_s q_s\int f_s(\mathbf{r},\mathbf{v},t)d^3v - \rho_{\text{ext}}(\mathbf{r},t). \tag{5}$$

The external fields satisfy also the electrostatic Maxwell equations and therefore in the electrostatic limit the internal field satisfies the Poisson equation

$$\varepsilon_0 \nabla \cdot \mathbf{E}_{\text{int}} = \sum_s q_s \int f_s(\mathbf{r}, \mathbf{v}, t) d^3 v = \sum_s q_s n_s = \rho(\mathbf{r}, t). \tag{6}$$

In the Vlasov–Poisson system the discreteness of plasma particles is lost, and the electric fields are found self-consistently from smoothed charge and current distributions. In addition the motion in the phase-space is incompressible, and f_s is constant in time along characteristics which are the single-particle trajectories in the presence of electromagnetic fields

$$\begin{aligned} &\frac{d\mathbf{r}_s(t)}{dt} = \mathbf{v}_s(t), \\ &m_s \frac{d\mathbf{v}_s(t)}{dt} = \frac{q_s}{m_s} [\mathbf{E}(\mathbf{r}_s(t), t) + \mathbf{v}_s \times \mathbf{B}_{\text{ext}}(\mathbf{r}_s(t), t)] \end{aligned} \tag{7}$$

We define also the species-mean molecular velocity $\mathbf{V}_s = \{V_{sx}, V_{sy}, V_{sz}\}$ by

$$\mathbf{V}_s(\mathbf{r}, t) \equiv \langle \mathbf{v} \rangle_s = \int_{-\infty}^{\infty} \mathbf{v} f_s(\mathbf{r}, \mathbf{v}, t) d\mathbf{v} / n_s(\mathbf{r}, t). \tag{8}$$

The mass-average velocity $\mathbf{V} = \{V_x, V_y, V_z\}$ used to represent the plasma as a single fluid is

$$\mathbf{V}(\mathbf{r}, t) = \sum_s n_s m_s \mathbf{V}_s / \sum_s n_s m_s. \tag{9}$$

The species diffusion velocity is defined as

$$\mathbf{W}_s = \mathbf{V}_s - \mathbf{V}. \tag{10}$$

The species s thermal (or random) velocity is given with respect to the species-mean velocity as

$$\mathbf{C}_s = \mathbf{v}_s - \mathbf{V}_s \tag{11}$$

or with respect to the mass-averaged velocity as

$$\mathbf{C}_s^* = \mathbf{v}_s - \mathbf{V} = \mathbf{C}_s + \mathbf{W}_s. \tag{12}$$

Physically significant moments of the distribution (macroscopic properties) can be derived using as the reference velocity the species-average velocity or the mass-average velocity [22–25]. The translational temperature is defined in species-mean system as T_s and in the mass-average system as T_s^* by

$$\frac{3}{2} k_B T_s^{(*)}(\mathbf{r}, t) = \frac{1}{2} m_p \left\langle C_s^{(*)2} \right\rangle \tag{13}$$

with $T_s^* = T_s + m_s W_s^2 / 3k_B$. Similarly, the scalar pressure is $p_s^{(*)}(\mathbf{r}, t) = n_s m_s \left\langle C_s^{(*)2} \right\rangle / 3$, the pressure tensor $\mathbf{P}_s^{(*)}(\mathbf{r}, t) = n_s m_s \left\langle \mathbf{C}_s^{(*)} \mathbf{C}_s^{(*)} \right\rangle$ and the heat flux vector is $\mathbf{q}_s^{(*)}(\mathbf{r}, t) = n_s m_s \left\langle C_s^{(*)2} \mathbf{C}_s^{(*)} \right\rangle / 2$. We define also single-fluid macroscopic variables for the plasma as follows:

$$\mathbf{J}(\mathbf{r}, t) = \sum_s n_s q_s \mathbf{V}_s = \rho \mathbf{V} + \sum_s n_s q_s \mathbf{W}_s, \tag{14}$$

$$T(\mathbf{r}, t) = \left(1 / \sum_s n_s \right) \sum_s n_s T_s + n_s m_s W_s^2 / 3k_B = \sum_s n_s T_s^* / \sum_s n_s, \tag{15}$$

$$p(\mathbf{r}, t) = \sum_s p_s^* = \sum_s p_s + \sum_s n_s m_s W_s^2 / 3, \tag{16}$$

$$P(\mathbf{r}, t) = \sum_s P_s^* = \sum_s P_s + \sum_s n_s m_s \mathbf{W}_s \mathbf{W}_s, \tag{17}$$

$$\mathbf{q}(\mathbf{r}, t) = \sum_s \mathbf{q}_s^* = \sum_s \mathbf{q}_s + (3/2) p_s \mathbf{W}_s + \mathbf{W}_s \cdot \mathbf{P}_s + (1/2) n_s m_s W_s^2 \mathbf{W}_s. \tag{18}$$

Other transport properties and macroscopic equations can be defined using either reference frame. As we discuss later in the paper, such moments of the distribution can be calculated directly from particle properties during a PIC simulation.

3. Unstructured particle-in-cell in 3D (UPIC3dE) methodology

The UPIC3dE method implements the conventional PIC computational steps on an unstructured Delaunay–Voronoi discretization. The UPIC3dE begins with the grid generation which provides an unstructured Delaunay mesh and its Voronoi dual. Computational particles are loaded in the domain and injected from boundaries. Charge is assigned from the position of the computational particles to the grid nodes. Gauss' integral law (4) is solved on the nodes in order to obtain the electric potential. The electric field is evaluated on the nodes and interpolated to the position of particles. Particles are moved according to Eq. (7). In addition, particles are allowed to enter or leave the domain based on specified boundary conditions.

Macroscopic single-fluid and multi-fluid variables are evaluated on nodes. The numerical implementation of the UPIC3dE steps on the unstructured Delaunay–Voronoi grid is discussed in the following sections.

3.1. Delaunay–Voronoi grid generation

The unstructured grid generator provides tetrahedral cells obtained through a Delaunay triangulation for arbitrary geometric configurations. The methodology [26] discretizes a domain Ω by N_D Delaunay tetrahedra and proceeds with a surface triangulation followed by a volume grid generation and subsequent optimization.

The surface triangulation is obtained with use of commercially available surface generators. The unstructured (volume) grid generator is based on Watson's incremental node insertion method [27], which uses properties of the Delaunay triangulation. An initial mesh is required for Watson's method, in order to have a domain where point insertion to begin. After the initial mesh is generated, the source geometry is inserted into the domain following two steps. First, the boundary nodes are successively inserted into the grid via Watson's algorithm. Second, the boundary facets present in the source geometry are recovered using local modifications to the grid. The cells external to the grid are removed as well as cells in any internal cavity.

The sizing function requires the interior of the grid to be enriched with nodes to the specified density. For this purpose the algorithm by Borouchaki and George [28] is implemented and extended to three dimensions [26]. In this algorithm, the characteristic distance between nodes is specified for each grid node as h. Every existing edge of the grid is divided into a number of new prospective nodes, so that the new resulting edge segments vary in length gradually between the h-values of the edge vertices. The prospective nodes are filtered in order to satisfy the spacing and grid quality criteria. Nodes falling too close to existing nodes are eliminated. Nodes that worsen grid quality as specified by the lowest dihedral angle in a set of cells are also discarded. The nodes that are not rejected are inserted into the grid via Watson's algorithm. The edge division process is repeated while new nodes are inserted.

An integration of two optimization techniques is implemented in order to improve the mesh quality. The first step involves mesh relaxation in order to obtain a mesh with the average node degree being as close to the optimal value as possible. It is reached by means of an edge-swapping procedure regardless of its effects on the Delaunay property of the mesh. The second step applies Laplacian smoothing by repositioning every node towards the average location of all adjacent nodes. At this point the mesh is no longer Delaunay and edge swapping may be necessary to recover this mesh property [26]. A quality improvement procedure has been implemented based on a user-defined minimum dihedral angle.

The UPIC3dE implementation requires local data structures for particle motion, and the sampling of macroscopic parameters. For ease of computational manipulation the grid parameters are stored in a data structure that maintains node position, node connectivity, face sharing and cell nearest-neighbor information. A Delaunay cell is illustrated in Fig. 1(a) and assigned a global cell index $D = 1, \ldots, N_D$. The N_d vertices of the cells are designated as the nodes of the domain. Each node is assigned with a global node index $d = 1, \ldots, N_d$ and has coordinates $\mathbf{r}_d = (x_d, y_d, z_d)$. The four nodes associated with a Delaunay cell D form a unique index set $\{J, K, L, M\}$ through an association $D \to \{J, K, L, M\}$ where the non-ordered set $\{J, K, L, M\} \in \{1, \ldots, N_d\}$. A node $\{J\}$ has coordinates $\mathbf{r}_J = (x_J, y_J, z_J)$ and the volume of the Delaunay cell is given

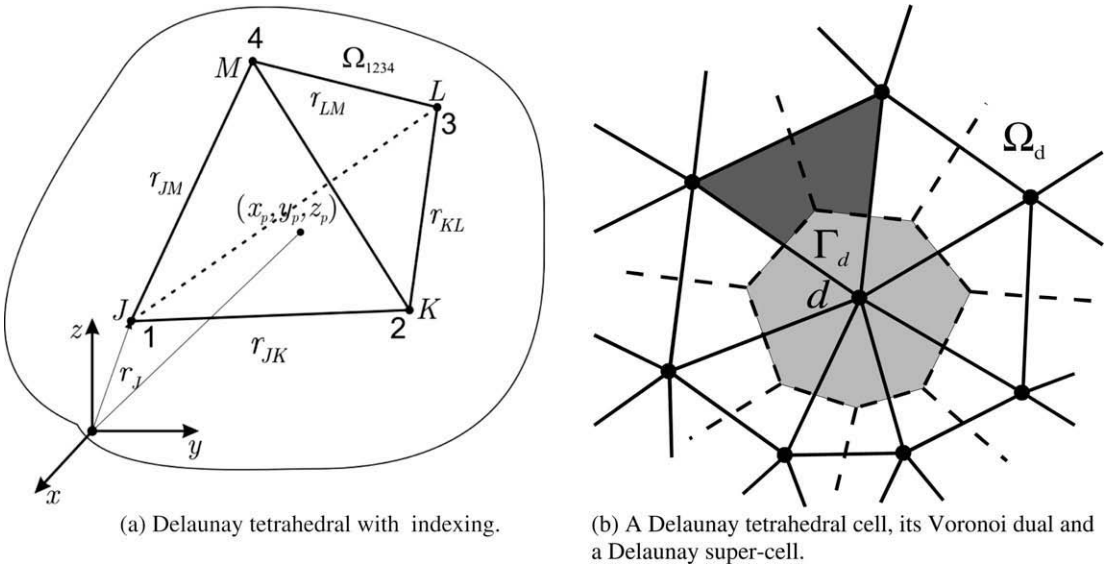

(a) Delaunay tetrahedral with indexing.

(b) A Delaunay tetrahedral cell, its Voronoi dual and a Delaunay super-cell.

Fig. 1. The Delaunay tetrahedron with global and local indexing in a domain Ω in 3d. A Delaunay cell, the Voronoi dual and a Delaunay supercell depicted in 2d.

$$\Omega_D \equiv \Omega_{JKLM} = \mathbf{r}_{MJ} \cdot (\mathbf{r}_{JK} \times \mathbf{r}_{JL})/6. \tag{19}$$

Each node d is associated with the Voronoi dual, Γ_d, and the Delaunay supercell Ω_d formed by all the Delaunay cells that share the node d as illustrated in Fig. 1(b) for a 2d geometry.

3.2. Particle loading

In UPIC3dE, loading is carried out by placing species s particles in each Delaunay cell with randomly chosen positions and velocities following the quasi-equilibrium, drifting Maxwellian distribution

$$f_{0s}(\mathbf{r}, \mathbf{v}, t) = n_s(\mathbf{r}, t)\left(\frac{m_s}{2\pi k T_s}\right)^{3/2} \exp\left[-\frac{m_s(\mathbf{v} - \mathbf{V}_s)^2}{2kT_s}\right], \tag{20}$$

where $n_s(\mathbf{r}, t), T_s(\mathbf{r}, t)$, and $\mathbf{V}_s(\mathbf{r}, t)$ are assumed as known. The number of computational particles loaded at each Delaunay cell is $C_D = n_s\Omega_D/F_N$, where F_N is the particle weight. The velocity components of each particle at $t = 0$ are sampled from (20) following the acceptance–rejection method [29]. The velocities of each particle at $t = 0$ are displaced backwards by $(-\Delta t/2)$ following the leaf-frog integration algorithm discussed in Section 3.8 and using the electric fields at $t = 0$ [1,30]. The determination of the particle's position in a Delaunay cell is carried out using a local vector coordinate system based on cell edges as shown in Fig. 2(a). Three vectors of random lengths along three cell-edges are generated by

$$\mathbf{a} = R_1^{1/3}\mathbf{r}_{12}, \quad \mathbf{b} = R_2^{1/2}R_1^{1/3}\mathbf{r}_{223}, \quad \mathbf{c} = R_3R_2^{1/2}R_1^{1/3}\mathbf{r}_{34}, \tag{21}$$

where R_1, R_2 and R_3 are random numbers. The local position vector, $\mathbf{P} = \mathbf{a} + \mathbf{b} + \mathbf{c}$ provides the particle's position from

$$\mathbf{r}_p = \mathbf{r}_1 + \mathbf{P}. \tag{22}$$

3.3. Particle injection at boundaries

Particles are injected into the domain at surfaces with certain attributes stored in a global array. For a general case, the inward flux of species s particles across a Delaunay boundary surface is due to a drifting Maxwellian equation (20)

$$\dot{N}_s = \frac{n_s}{2\beta_s\sqrt{\pi}}(\exp(-S_s^2\cos^2(\theta)) + \sqrt{\pi}S_s\cos(\theta)\{1 + \mathrm{erf}(S_s\cos(\theta))\}), \tag{23}$$

where $\beta_s = \sqrt{m_s/(2k_BT_s)}$, the mean velocity $\mathbf{V}_s$ is inclined at an angle θ to the unit normal vector $\mathbf{e}$ and the speed ratio is

$$S_s = V_s\beta_s. \tag{24}$$

The number of computational particles to be injected to the domain in a given time-step, ΔN_p, is $\Delta N_p = \dot{N}_p\Delta tA_s/F_N$, where Δt is the time-step and A_s is the area of the surface element. The calculation of the injection position bounded by two face edge lengths is carried out using localized coordinates generated from the face edges of a Delaunay, as shown in Fig. 2(b). Two vectors of random length are determined from the respective defining edge as

$$\mathbf{a} = R_1^{1/2}\mathbf{r}_{12}, \quad \mathbf{b} = R_2R_1^{1/2}\mathbf{r}_{23}. \tag{25}$$

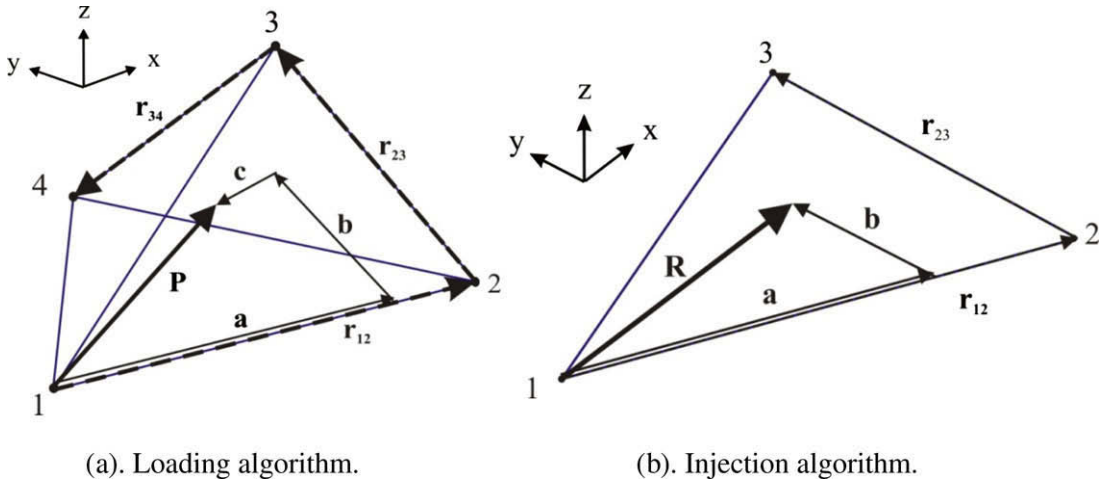

Fig. 2. Particle position calculation geometry used in the loading algorithm and injection algorithm of the UPIC3dE method.

The local position vector, $\mathbf{R} = \mathbf{a} + \mathbf{b}$ provides the particle's injection position from

$$\mathbf{r}_p = \mathbf{r}_1 + \mathbf{R}. \tag{26}$$

The generation of the velocity from Eq. (20) follows the acceptance–rejection algorithm [29]. To apply properly the leap-frog particle integration algorithm and reduce numerical errors, the velocities are moved backwards by $(-\Delta t/2)$ using the electric fields at the current time [1,31].

3.4. Charge assignment and force interpolation

The hierarchy of charge assignment functions (or weights) in UPIC3dE is derived following Hockney and Eastwood [2] according to the long-range, smoothness, and momentum conservation constraints. Using a local index set each Delaunay tetrahedron Ω_{1234} is defined by four nodes with $\mathbf{r}_I$ $(I = 1,\ldots,4)$ as shown in Fig. 1(a). For a particle in a position $\mathbf{r}_p = (x_p, y_p, z_p) \in \Omega_{1234}$ the charge is assigned to the four nodes associated with the Delaunay Ω_{1234} with functions $W_I(x_p, y_p, z_p),\ I = 1,\ldots,4$. Following [2] we assume that the potential at position $\mathbf{r}$ due to the unit charge in node position $\mathbf{r}_I \in \Omega_I$ is given by the Green's function $G(r - r_I)$. The potential at $r \equiv (x, y, z)$ due to the charges at M grid points is given by

$$\phi(x,y,z) = \sum_{I=1}^{4} W_I(x_p, y_p, z_p) G(r - r_I). \tag{27}$$

Taylor expanding $G(r - r_I)$ about $(r - r_p)$ and assuming that $G(\mathbf{r}') = G(r')$

$$\begin{aligned}\phi(x,y,z) = \sum_{I=1,4} W_I(x_p,y_p,z_p) G(r - r_p) + \sum_{I=1,4} W_I(x_p,y_p,z_p) \Bigg[(x_p - x_I)\frac{dG(r_p - r)}{dx_p} + (y_p - y_I)\frac{dG(r_p - r)}{dy_p} \\ + (z_p - z_I)\frac{dG(r_p - r)}{dz_p} + \mathrm{O}\{(x_p - x_I)^2, (y_p - y_I)^2, (z_p - z_I)^2\} \Bigg].\end{aligned} \tag{28}$$

Charge conservation requires that

$$\sum_{I=1}^{4} W_I(x_p, y_p, z_p) = 1. \tag{29}$$

The requirement that the first-order terms in the expansion Eq. (28) are grid independent provides the first-order constraint as

$$\begin{aligned}&\sum_{I=1,4} W_I(x_p,y_p,z_p)(x_p - x_I) = 0,\\ &\sum_{I=1,4} W_I(x_p,y_p,z_p)(y_p - y_I) = 0,\\ &\sum_{I=1,4} W_I(x_p,y_p,z_p)(z_p - z_I) = 0.\end{aligned} \tag{30}$$

With the Nearest Grid Point (NGP) scheme, the charge from the particle at position $r_p = (x_p, y_p, z_p) \in \Omega_{1234}$ is assigned to closest node according to

$$\begin{aligned}&W_1(\mathbf{r}_p) = 1 \quad \text{if } \min|\mathbf{r}_{1,2,3,4} - \mathbf{r}_p| = |\mathbf{r}_1 - \mathbf{r}_p|,\\ &W_2(\mathbf{r}_p) = W_3(\mathbf{r}_p) = W_4(\mathbf{r}_p) = 0.\end{aligned} \tag{31}$$

With the Cloud In Cell (CIC) scheme, the charge from the particle p at position $\mathbf{r}_p \equiv (x_p, y_p, z_p) \in \Omega_{1234}$ is assigned to the four nodes of the Delaunay cell. Solution to the system of constraints (29) and (30) provides the weight functions

$$W_1 = \frac{\Omega_{P234}}{\Omega_{1234}}, \quad W_2 = \frac{\Omega_{P134}}{\Omega_{1234}}, \quad W_3 = \frac{\Omega_{P124}}{\Omega_{1234}}, \quad W_4 = \frac{\Omega_{P123}}{\Omega_{1234}}, \tag{32}$$

where Ω_{Pklm} is the volume of the tetrahedron formed by the particle p and nodes $1, 2, 3$

$$\Omega_{P234} = [\mathbf{r}_{4p} \cdot (\mathbf{r}_{p2} \times \mathbf{r}_{23})]/6. \tag{33}$$

Implementation of the CIC weights on the 3-D unstructured tetrahedral grid is therefore analogous to a volume-weighing and is represented graphically in Fig. 1(a).

3.5. Nodal number density and charge density

The evaluation of the number density n_{sd} and charge density ρ_{sd} of species s particles at a node d with $r_d = (x_d, y_d, z_d)$ utilizes the Delaunay–Voronoi dual in order to implement the PIC approach used with structured grids [1,3]. All species s particles residing in a Delaunay cell are weighted to the four nodes $D \to \{J, K, L, M\}$ following the NGP or the CIC scheme. This

algorithmic procedure applied to each Delaunay cell $D = 1, \ldots, N_D$ provides the total weight W_{sd} and total charge Q_{sd} of species s for each node $d = 1, \ldots, N_d$. Similar to structured grids, contribution to a node d comes from particles that reside in the cells that share the node. In our unstructured grid these shared cells define the Delaunay supercell Ω_d depicted in Fig. 1(b). The species s number density at the a node d is obtained using the volume of the Voronoi dual Γ_d shown in Fig. 1(b), as

$$n_s(x_d, y_d, z_d) \equiv n_{sd} = F_s W_{sd}/\Gamma_d. \tag{34}$$

Similarly, the species s charge density at a node d is

$$\rho_s(x_d, y_d, z_d) \equiv \rho_{sd} = Q_{sd}/\Gamma_d. \tag{35}$$

3.6. Nodal electric potential

The electric potential is obtained through an approach that takes advantage of the Delaunay–Voronoi dual. The formulation is based on the integral Gauss law (4) using as the Gaussian surface the Voronoi volume Γ_d associated with a node shown in Fig. 3 as

$$\oint\!\!\oint_S \mathbf{E} \cdot d\mathbf{S} = \frac{1}{\varepsilon_o} \int\int\int_\Gamma \rho d\Gamma. \tag{36}$$

The semi-discrete form of Gauss' law is

$$\sum_{k=1}^{N_f} \mathbf{E}_{dk} \cdot (\mathbf{n}A)_{dk} = Q_d/\varepsilon_0, \tag{37}$$

where N_f is the number of corresponding faces of the Voronoi Γ_d, $\mathbf{E}_{dk}$ is the field over the area A_{dk}, and Q_d is the charge at node d enclosed in Γ_d. Using the potential Φ and the definition of the gradient, Eq. (37) becomes

$$\sum_{k=1}^{N_f} \nabla\Phi_{dk} \cdot (\hat{\mathbf{n}}A)_{dk} = \sum_{k=1}^{N_f} \left(A\frac{\partial\Phi}{\partial n}\right)_{dk} = -\frac{Q_d}{\varepsilon_0}. \tag{38}$$

The derivative of the potential at a face of a Voronoi cell can be obtained from

$$\left.\frac{\partial\Phi}{\partial n}\right|_{dk} = \frac{\Phi_k - \Phi_d}{L_{dk}} + O(L_{dk}^2/4), \tag{39}$$

where L_{dk} is the length of the Delaunay cell indicated in Fig. 3(a). Eq. (38) then becomes

$$\sum_{k=1}^{N_f} \nabla\Phi \cdot (\hat{\mathbf{n}}A)_{dk} = \sum_{k=1}^{N_f} (\Phi_d - \Phi_k)\frac{A_{dk}}{L_{dk}} = \frac{Q_d}{\varepsilon_0}. \tag{40}$$

Applying (40) to all the nodes N_d in the domain, a system of $N_d \times N_d$ linear equations is obtained

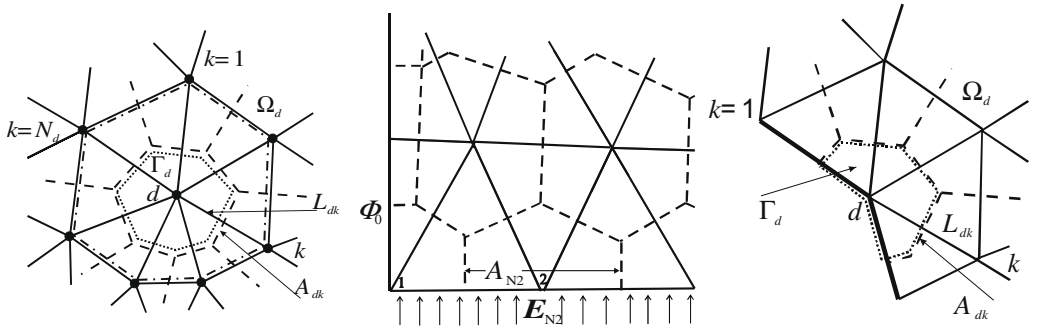

(a). The Gaussian surface Γ_d (dot), the Voronoi Γ_d (dash), and the Delaunay super-cell Ω_d (dash-dot), used in the evaluation of the potential and electric fields at a node d.

(b). Dirichlet (Φ_0) and Neumann ($\boldsymbol{E}_{N2}$) boundary conditions.

(c). Floating conductor with the Gaussian surface Γ_d (dot).

Fig. 3. Cell structure used in the finite-volume discretization of Gauss' integral law in UPIC3dE for a 2d geometry.

$$\begin{bmatrix} R_{11} & R_{12} & R_{13} & \cdots & R_{1N_d} \\ R_{2,1} & R_{2,2} & R_{2,3} & \cdots & R_{2N_d} \\ R_{31} & R_{32} & R_{33} & \cdots & R_{3N_d} \\ \vdots & \vdots & \vdots & \ddots & \vdots \\ R_{N_d1} & R_{N_d2} & R_{N_d3} & \cdots & R_{N_dN_d} \end{bmatrix} \begin{Bmatrix} \Phi_1 \\ \Phi_2 \\ \Phi_3 \\ \vdots \\ \Phi_{N_d} \end{Bmatrix} = \frac{1}{\varepsilon_0} \begin{Bmatrix} Q_1 \\ Q_2 \\ Q_3 \\ \vdots \\ Q_{N_d} \end{Bmatrix}. \tag{41}$$

For global node indexes $I = 1, \ldots, N_d$ and $J = 1, \ldots, N_d$ the coefficients R_{IJ} are given by

$$\begin{aligned} R_{IJ} &= \sum_{k=1}^{N_f} A_{Ik}/L_{Ik} \quad \text{for } I = J, \\ R_{IJ} &= -A_{Ik}/L_{Ik} \quad \text{if } (I,J) \in \Omega_d, \\ R_{IJ} &= 0 \quad \text{if} (I,J) \notin \Omega_d. \end{aligned} \tag{42}$$

The sparse matrix in Eq. (41) is stored using the compressed sparse row scheme [32, Sections 3 and 6] and the solution to the linear system of equations is obtained using the Jacobi or the Generalized Minimize Residual (GMRES) method [32, Sections 4 and 6].

3.6.1. Dirichlet, Neumann, and floating potential boundary conditions

The implementation of Dirichlet and Neumann boundary conditions is depicted in Fig. 3(b) for a 2d configuration. The boundaries of the Delaunay triangles, surfaces in 3d, coincide with the boundaries of the Voronoi and therefore. In Fig. 3(b) node-1 has a potential Φ_o while node-2 is a Neumann boundary associated with and the applied inward normal electric filed E_{N2}. The application of the matrix equation (41) leads

$$\begin{bmatrix} 1 & 0 & 0 & \cdots & 0 \\ R_{2,1} & R_{2,2} & R_{2,3} & \cdots & R_{2N_d} \\ R_{31} & R_{32} & R_{33} & \cdots & R_{3N_d} \\ \vdots & \vdots & \vdots & \ddots & \vdots \\ R_{N_d1} & R_{N_d2} & R_{N_d3} & \cdots & R_{N_dN_d} \end{bmatrix} \begin{Bmatrix} \Phi_1 \\ \Phi_2 \\ \Phi_3 \\ \vdots \\ \Phi_{N_d} \end{Bmatrix} = \frac{1}{\varepsilon_0} \begin{Bmatrix} \Phi_o \\ Q_2 + \varepsilon_o E_{N2} A_{N2} \\ Q_3 \\ \vdots \\ Q_{N_d} \end{Bmatrix}. \tag{43}$$

Bounded plasmas interact with surfaces often connected to external circuits. For a floating conductor, i.e. an electrode that does not exchange charge with the external circuit, the time variation of the total charge density inside the volume is obtained from the charge conservation equation [33,17],

$$\oint_S \mathbf{J} \cdot d\mathbf{S} = \frac{d}{dt} \iiint_V \rho dV \tag{44}$$

The discrete form of Eq. (44) is

$$A(\sigma_T(t) - \sigma_T(t - \Delta t)) = Q^{con}(t) \tag{45}$$

where, σ_T is a total charge density on the surface of the conductor, A is the conductor surface area exposed to the plasma, Q^{con} is convective charge collected by the conductor for the time $t - \Delta t$ to t due to particles from the plasma. The finite-volume discretization of Gauss' law involves a Gaussian surface that coincides with the Voronoi volume associated with the boundary node b and includes the area just below the surface of the conductor as shown for a 2d case in Fig. 3(c). Application of Eq. (40) provides

$$\varepsilon_0 \left(\sum_k^{N_f} (\Phi_b - \Phi_k) \frac{A_{dk}}{L_{dk}} \right) = Q_b^{pl} + \sigma_b A_b. \tag{46}$$

In this formulation A_b is the boundary area associated with a boundary node b, Q_b^{pl} is the total charge assigned to the node b due to the plasma and $A_b\sigma_b$ is the surface charge. The summation is carried over all the faces of the Voronoi but clearly the boundary nodes on the conductor that have potential $\Phi_b = \Phi_k$ do not contribute to the summation. Summing Eq. (46) for all boundary nodes b of the floating conductor and substituting Eq. (46) into Eq. (45) it becomes

$$A\sigma_T(t) = A\sigma_T(t - \Delta t) + Q^{con}(t) = \sum_b \left(\varepsilon_0 \left(\sum_k (\Phi_b(t) - \Phi_k(t)) \frac{A_{bk}}{L_{bk}} \right) - Q_b^{pl}(t) \right) \tag{47}$$

All boundary nodes of the conductor have the same constant potential $\Phi_d(t)$ therefore,

$$\Phi_b(t) = \frac{\frac{1}{\varepsilon_0} \left(A\sigma_T(t - \Delta t) + Q^{con}(t) + \sum_d Q_b^{pl}(t) \right) + \sum_b \left(\sum_k \Phi_k(t) \frac{A_{bk}}{L_{bk}} \right)}{\sum_b \sum_k \frac{A_{bk}}{L_{bk}}} \tag{48}$$

The summation is carried for all nodes that have potential $\Phi_b(t) \neq \Phi_k(t)$. This expression contains unknown terms $\Phi_k(t)$ and requires successive iteration between the solution of Gauss' law Eq. (41) and Eq. (48). We follow in this work an alternative approach that uses the superposition principle to find an explicit relation for the potential on the floating boundary [17]. The total electrostatic potential at any node to be expressed as

$$\Phi_d(t) = \Phi_d^{pla}(t) + \Phi_b(t)\tilde{\Phi}_d \tag{49}$$

In the above, $\Phi_k^{pla}(t)$ is the Poisson potential due to the volume charge in the plasma and zero boundary conditions. This potential is obtained at every time t through the solution of Eq. (41) with all boundary nodes set to zero potential. The term $\tilde{\Phi}_d$ is the normalized, time-independent Laplacian potential due to the boundary conditions and without space-charge. This potential is obtained once through the solution of Eq. (41) with all volume charges set to zero and the potential on the nodes of the floating conductor set to unity. By substitution of Eq. (49) with $d \equiv k$ into (48) we obtain an explicit relation,

$$\Phi_0(t) = \frac{\frac{1}{\varepsilon_0}\left(A\sigma_T(t-\Delta t) + \sum_b Q_{con}(t) + Q_b^{pla}(t)\right) + \sum_b\left(\sum_k \Phi_k^{pla}(t)\frac{A_{bk}}{L_{bk}}\right)}{\sum_b\sum_k \frac{A_{bk}}{L_{bk}}(1-\tilde{\Phi}_b)}. \tag{50}$$

With the potential on the conductor known the total surface charge on the conductor $A\sigma_T(t)$ is evaluated using Eq. (47).

3.7. Nodal electric field

The integral theorem

$$\int\int\int_V \nabla\Phi\, dV = \oiint_S \Phi\, d\mathbf{S} \tag{51}$$

applied to the potential $\Phi(x,y,z)$ provides the definition of the electric field as

$$\nabla\Phi = \lim_{V\to 0}\frac{\oiint_s \Phi\, d\mathbf{S}}{V} = -\mathbf{E}. \tag{52}$$

The theorem (51) can be derived from the divergence theorem [34, Chapter 11.8.2]. The discrete form of Eq. (52) provides the average value of the $\nabla\Phi$ in a volume V_d and the electric field at node d as

$$\overline{\nabla\Phi}_d = \frac{1}{V_d}\sum_{f=1}^{n}\Phi_f\mathbf{S}_f \equiv -\mathbf{E}_d. \tag{53}$$

The volume V_d can associated with the Voronoi, $V_d = \Gamma_d$ or the Delaunay supercell, $V_d = \Omega_d$, as indicated in Fig. 3(a) for a 2d case. In Eq. (53) $\mathbf{S}_f$ is the area and Φ_f is the potential of the cell face f. For a Voronoi cell the face potential Φ_f is the average of the vertices that form a face. For a Delaunay supercell Φ_f is the average of the potential on the vertices (nodes) that form that face.

3.8. Integration of particle motion

The equations of particle motion (7) are integrated following Buneman's time-centered leapfrog formulation [35]

$$\frac{\mathbf{v}_p^{t+\Delta t/2} - \mathbf{v}_p^{t-\Delta t/2}}{\Delta t} = \frac{q_p}{m_p}\left[\mathbf{E}^t(\mathbf{r}_p) + \frac{\mathbf{v}_p^{t+\Delta t/2} - \mathbf{v}_p^{t-\Delta t/2}}{2}\times\mathbf{B}_{ext}^t(\mathbf{r}_p)\right], \tag{54}$$

$$\mathbf{r}_p^{t+\Delta t} = \mathbf{v}_p^{t+\Delta t/2}\Delta t + \mathbf{r}_p^t \tag{55}$$

combined with Boris's algorithm [36] for the implementation of the $\mathbf{v}\times\mathbf{B}_{ext}$ rotation [1, Chapter 4.3]. The electric field at the position of the particle $\mathbf{r}_p = (x_p, y_p, z_p)$ residing in the Delaunay Ω_{1234} is obtained through interpolation from the four nodes of the tetrahedral cell as

$$\mathbf{E}(x_p,y_p,z_p) = \sum_{I=1,4}\mathbf{E}(x_I,y_I,z_I)W_I(x_p,y_p,z_p). \tag{56}$$

Following [1] the weights in force interpolation are identical to those obtained for the charge assignment (31) and (32). Stability conditions are derived using the Von Neumann analysis [37, Chapter 8]. The amplification matrix

$$\begin{Bmatrix}\mathbf{v}^{t+\Delta t/2}\\ \mathbf{r}^{t+\Delta t/2}\end{Bmatrix} = G\begin{Bmatrix}\mathbf{v}^{t-\Delta t/2}\\ \mathbf{r}^{t-\Delta t/2}\end{Bmatrix} \tag{57}$$

has eigenvalues

$$\lambda_{1,2,3} = \frac{1}{2}\left(2-\omega_p^2\Delta t^2 + \omega_p\Delta t\sqrt{\omega_p^2\Delta t^2-4}\right), \quad \lambda_{4,5,6} = \frac{1}{2}\left(2-\omega_p^2\Delta t^2 - \omega_p\Delta t\sqrt{\omega_p^2\Delta t^2-4}\right), \tag{58}$$

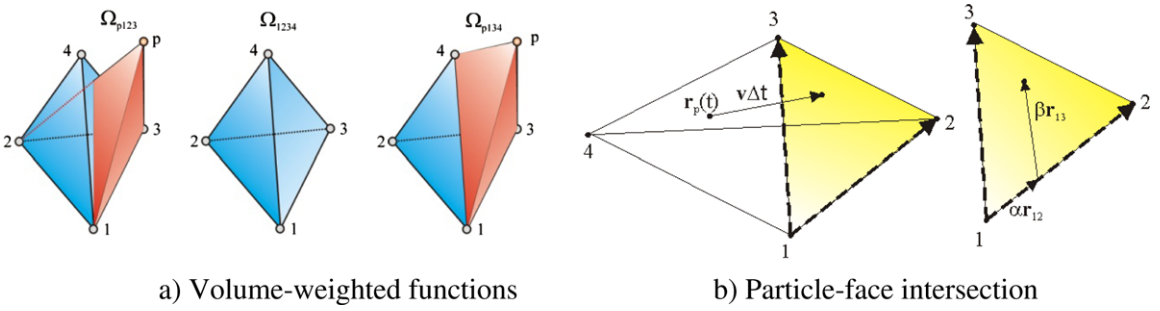

Fig. 4. Geometries utilized with the particle motion algorithm.

where the plasma frequency $\omega_p = \sqrt{n_e e^2/\varepsilon_0 m_e}$. For stability

$$|\lambda|_{\max} \leqslant 1 \tag{59}$$

and one recovers the well-known condition for a cold plasma and uniform grid given in [1] as $\omega_p \Delta t < 2$.

3.9. Particle search-locate algorithm (particle tracer)

Identification of the cell in which a particle resides in unstructured grids can be a computational intensive procedure. We developed an algorithm for the Delaunay–Voronoi grid based on the successive-neighbor particle search methodology of Löhner and Ambrosiano [18]. Following Fig. 4, the particle with $\mathbf{r}_p(t)$ resides in a Delaunay cell with volume Ω_{1234} and at $t + \Delta t$ moves to position $\mathbf{r}_p(t + \Delta t)$. The algorithm requires the evaluation of volume-weighted functions N_1, N_2, N_3, N_4 obtained from the new particle position $\mathbf{r}_p(t + \Delta t)$ with respect to the nodes of the Delaunay cell of origin. The steps are outlined below:

(S.1) Calculate the weight functions

$$N_1(\mathbf{r}_p(t+dt)) = \frac{\Omega_{p234}}{\Omega_{1234}} = \frac{[\mathbf{r}_{24} \cdot (\mathbf{r}_{2p} \times \mathbf{r}_{23})]/6}{[\mathbf{r}_{14} \cdot (\mathbf{r}_{12} \times \mathbf{r}_{23})]/6}, \quad N_2(\mathbf{r}_p(t+dt)) = \frac{\Omega_{p134}}{\Omega_{1234}},$$

$$N_3(\mathbf{r}_p(t+dt)) = \frac{\Omega_{p124}}{\Omega_{1234}}, \quad N_4(\mathbf{r}_p(t+dt)) = \frac{\Omega_{p123}}{\Omega_{1234}}.$$

(S.2) If $N_1 + N_2 + N_3 + N_4 = 1$ then $\mathbf{r}_p(t + dt) \in \Omega_{1234}$.

(S.3) If $N_1 + N_2 + N_3 + N_4 > 1$ then $\mathbf{r}_p(t + dt) \notin \Omega_{1234}$ and cells adjacent to Ω_{1234} should be searched. In order to find the tetrahedron to be searched, the face with which the particle has intersected needs to be identified. For example, intersection of a computational particle p with a face (1–2–3) requires that

$$\mathbf{r}_p(t) + \mathbf{v}_p(t)\tau = \alpha \mathbf{r}_{21} + \beta \mathbf{r}_{32}. \tag{60}$$

In the above vector equation τ is a time it takes for the particle to move from its initial position to the face (1–2–3) and the coefficients α and β define the point of intersection in the skewed coordinate system. The resulting system of scalar equations may be ill-conditioned if the cell is ill-shaped or if the velocity of the particle is very large. The algorithmic implementation is as follows:

(S.4) For cell face (1–2–3) solve the system of linear equations

$$\mathbf{r}_p(t) + \mathbf{v}_p(t)\tau = \alpha \mathbf{r}_{21} + \beta \mathbf{r}_{32}. \tag{61}$$

(S.6) If $\alpha + \beta > 1$ then intersection occurred with face (1–2–3) and the algorithmic steps (S.1)–(S.4) are repeated for the tetrahedron that shares this face.

(S.5) If τ is negative or $1 < \alpha, \beta < 0$ then the intersection does not occur and then next face is investigated.

3.10. Evaluation of macroscopic plasma properties

Other macroscopic (fluid) properties can be evaluated at each node d of the domain. The species-velocity (8), mass-average velocity (13) and single-fluid plasma properties (14)–(18) are obtained from simple averaging of the particles that reside in the Voronoi dual Γ_d. As these macroscopic properties are used for diagnostic purposes there is no weighting procedure involved. For example for N_{sd} total number species s particles in the Voronoi cell Γ_d the species mean molecular velocity (8) is

$$\mathbf{V}_{sd} = \sum_{p=1}^{N_{sd}} F_s \mathbf{v}_{ps} / N_{sd} F_s \tag{62}$$

and the species translational temperature (13) is

$$T_s^{(*)}(\mathbf{r},t) = \frac{1}{3k_B} m_s \sum_{p=1}^{N_{sd}} F_s C_{ps}^{(*)2} / N_{sd} F_s. \tag{63}$$

4. Error analysis of the UPIC3dE methodology

In particle-in-cell (PIC) simulations the orbits of the particles are perturbed from the true orbits and collisions in the simulation occur at rates different than the real plasma. This is a result of the smaller of number of particles in the simulation than in the real space, the effects of spatial discretization, the charge and force interpolation, and time integration. Hockney [19] provided the theory for measuring the numerical error in 2D-3V PIC simulations with uniform grids using the concepts of heating, slowing-down and deflection times. We extend this approach in 3D-3V space and study the numerical heating and collisions for the UPIC3dE methodology.

A typical computational domain used in the heating calculations is shown in Fig. 5. The plasma is loaded initially into the spherical domain following an quasi-equilibrium Maxwellian distribution equation (20) with $n_e = n_i = 10^{16}\ \mathrm{m}^{-3}, T_e = T_i = 2$ eV, and zero drift velocity. Electrons and ions are also injected at each time-step from the open boundaries following Eq. (20). Zero electric field is set at the open boundaries of the domain. Particles that reach the domain boundaries are removed from the simulation. Following Hockney [19] we designate the initial velocity of the particle p as the parallel direction for that particle $\mathbf{v}_p(0) = \mathbf{v}_{p\|}(0)$. In a UPIC3dE simulation we measure at time t for a particle p its velocity $\mathbf{v}_p(t)$, its velocity component in the parallel direction

$$\mathbf{v}_{p\|}(t) = \mathbf{v}_p(t) \cdot \mathbf{v}_{p\|}(0) / |\mathbf{v}_{p\|}(0)|, \tag{64}$$

its velocity component in perpendicular direction

$$\mathbf{v}_{p\perp}(t) = \mathbf{v}_p(t) - \mathbf{v}_{p\|}(t) \tag{65}$$

and the deflection angle $\varphi_p(t)$

$$\varphi_p(t) = \cos^{-1}(\mathbf{v}_p(0) \cdot \mathbf{v}_p(t) / |\mathbf{v}_p(0)||\mathbf{v}_p(t)|). \tag{66}$$

The change in the kinetic energy of a particle p of species s at the time t from its initial value is ΔE_p, and the average change of the kinetic energy of a particle of species s in the ensemble

$$\langle \Delta E_s(t) \rangle = \frac{1}{N_s} \sum_{p=1}^{N_s} \Delta E_p(t) = \frac{1}{N_s} \sum_{p=1}^{N_s} \frac{1}{2} m_p (\mathbf{v}_p^2(t) - \mathbf{v}_p^2(0)). \tag{67}$$

The heating time τ_{Hs} is defined as the time for the average kinetic energy per particle of species s to increase its energy by $k_B T_s/2$,

$$\langle \Delta E(\tau_{Hs}) \rangle = k_B T_s(0)/2. \tag{68}$$

An interpretation of heating can be provided by using the a stochastic error field, $\delta\mathbf{E}$ that accounts for all errors associated with a PIC simulation. It can be sown [2, Section 9] that for n timesteps

$$\langle \Delta E_s(t) \rangle = \frac{1}{2} \frac{q_s^2}{m_s} (\Delta t)^2 |\delta\mathbf{E}|^2 n. \tag{69}$$

Heating therefore, increases with increasing Δt or increasing number of iterations. Eq. (69) shows that the main contribution to heating comes from electrons.

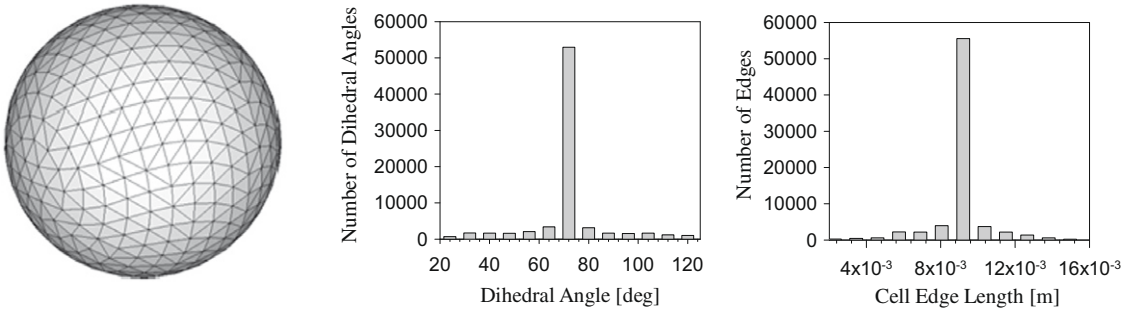

(a) Computational domain (b) Dihedral ditribution (c) Grid size distribution

Fig. 5. Computational domain used for the evaluation of heating, slowing-down and deflection times in the UPIC3dE simulations.

Previous 1d and 2d PIC investigations on uniform grids [38–40] have shown that τ_H strongly depends on $\omega_p\Delta t$ and $\Delta r/\lambda_D$, the ratio of the size of the computational cell over the Debye length,

$$\lambda_D = \sqrt{\varepsilon_o kT_e/e^2 n_e}. \tag{70}$$

The relevant cell size in our study is the edge length of a tetrahedron, Δr, as shown in Fig. 1. To generate a grid with tetrahedrals of nearly equal Δr the cells should have approximately the same volume and dihedral angles as close to 70.53°. Fig. 5 shows the histograms for the dihedral angles and edge lengths obtained for a typical grid used it these simulations.

Fig. 6(a) shows the effects on heating time from varying the parameter $v_{Te}\Delta t/\Delta r$, where $v_{Te} = \langle C_e^2\rangle^{1/2}$ while keeping the number of particles per cell constant. The heating time is normalized with the plasma frequency ω_p. One can observe than when $v_{Te}\Delta t/\Delta r$ is in the range of 10^{-4} to 5×10^{-4} the heating time remains almost constant. For both the NGP and CIC weighting schemes the simulations show a significant decrease in $\omega_p\tau_H$ from 5×10^{-4} to 10^{-3}. Further increase of the timestep has no impact on $\omega_p\tau_H$. The increase in the timestep leads in general to a larger stochastic error $|\delta\mathbf{E}|$ and as such smaller heating times according to Eq. (69). The results show that the CIC heating time is about 20% larger than the NGP heating time for small timesteps $v_{Te}\Delta t/\Delta r < 5\times10^{-4}$. For large timesteps, $v_{Te}\Delta t/\Delta r > 5\times10^{-4}$, this difference is more than 100%. The CIC weighting is associated with smaller error $|\delta\mathbf{E}|$ than the NGP weighting and therefore, to results in larger heating times.

Another parameter varied in the heating time investigation is the number of computational particles per cell, C_D. An increase in C_D leads to smoother electric fields, smaller $|\delta\mathbf{E}|$ and therefore larger heating times. Fig. 6(b) shows the effect of C_D on the heating time for NGP and linear weighting schemes. The increase in the heating time shown is about 10 times for both weighting schemes while C_D varies from 15 to 90. It is important to mention that the computational time for the particle-move scales linearly with the number of particles. Therefore, a tradeoff is required between the overall computational time and the quality of the computation.

The ratio of the Debye length to the cell edge length $\lambda_D/\Delta r$ has a strong effect on the heating time as shown in Fig. 6(c). A decrease of the heating time by an order of magnitude is observed when $\lambda_D/\Delta r$ decreases from 0.2 to 2. There is no appreciable effect on heating in the range $2 \leqslant \lambda_D/\Delta r \leqslant 5$. When $\lambda_D/\Delta r$ is increased further Fig. 6(c) shows a decrease in the heating time by an almost order of magnitude. There is no impact of the weighting scheme on the heating time.

The plasma in the simulation can be treated as collisionless for simulation times that are less than the numerical slowing-down time τ_S defined as

$$\langle v_{s\|}(\tau_S)\rangle = \frac{1}{N_s}\sum_{p=1}^{N_s} v_{p\|}(\tau_S) = \langle v_{s\|}(0)\rangle/\exp(1). \tag{71}$$

Since the average electron slowing-down time is much smaller than the slowing-down time for heavier ions, it is used in UPIC3dE to define the limiting conditions. Fig. 7 shows the slowing-down time normalized with the electron–ion collision time for a fully ionized plasma τ_{ei} [41] as the function of the number of particles per computational cell for the NGP and CIC weighting schemes. The slowing-down time exhibits a linear growth as the number of computational particles in the domain increases. The magnitude of the slowing-down time does not have any significant dependence on the order of the weighting scheme used.

The deflection time relates also to numerical collisions [19]. Using Eq. (66) we calculate the root-mean-square average deflection for a particle of species s at time t

$$\sqrt{\langle\phi_s^2(t)\rangle} = \sqrt{\frac{1}{N_s}\sum_{p=1}^{N_s}\phi_{sp}^2(t)} \tag{72}$$

and define the deflection time τ_Φ as the time for the average deflection to reach 90°,

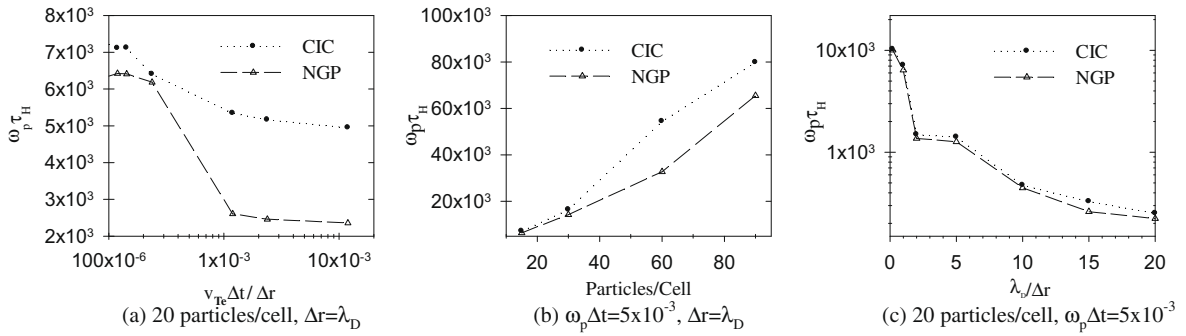

(a) 20 particles/cell, $\Delta r=\lambda_D$ (b) $\omega_p\Delta t=5\text{x}10^{-3}$, $\Delta r=\lambda_D$ (c) 20 particles/cell, $\omega_p\Delta t=5\text{x}10^{-3}$

Fig. 6. Heating time in UPIC3dE simulations showing the effects of time step, particle/cell and grid size.

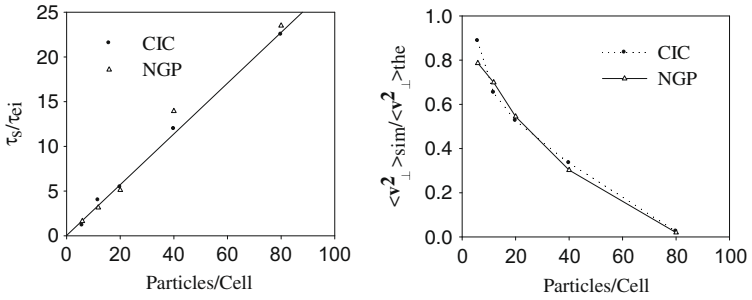

Fig. 7. Slowing-down and deflection time in UPIC3dE simulations showing the effects of particle loading for zero-order (NGP) and first-order (CIC) weighting schemes.

$$\sqrt{\langle \varphi_s^2(\tau_\Phi)\rangle} = \pi/2. \tag{73}$$

The average change in the perpendicular velocity component $\langle \mathbf{v}_\perp^2 \rangle_{sim}$ is evaluated when the average value of the deflection angle of an electron reaches 90°. This value is compared to the theoretical value $\langle \mathbf{v}_\perp^2 \rangle_{the}$ [41]. Fig. 7(b) shows $\langle \mathbf{v}_\perp^2 \rangle_{sim}/\langle \mathbf{v}_\perp^2 \rangle_{the}$ as a function of the number of particles per computational cell. The rate of change of the perpendicular component of the velocity decreases significantly with an increase of number of particles. Since the deflection time is much smaller than heating time, no significant dependence upon the type of weighting scheme is observed.

5. Validation of the UPIC3dE methodology

The UPIC3dE methodology is applied to the simulation of current collection by cylindrical Langmuir probes of length L_p and radius r_p in collisionless, stationary and drifting, fully ionized, unmagnetized plasmas characterized by a Maxwellian distribution equation (20). The UPIC3dE results are compared to the numerical predictions by Laframboise [42], analytical approximations by Peterson and Talbot [43], and analytical solutions by Kanal [44], and Johnson and Murphree [45].

The parameters for the UPIC3dE simulations are specified in Table 1. The size of the computational domain indicated by the radius R_D is set so that the potential at the boundaries reaches zero, i.e., the unperturbed value of the space (or plasma) potential, Φ_s. Examples of the computational domains used are shown in Fig. 8 indicating the vastly different requirements needed to capture the thin-sheath ($r_p \gg \lambda_D$) and orbital-motion limited (OML) ($r_p \ll \lambda_D$) regimes of operation. For cases 1.1–2.2 the cells are almost equal in volume with edge lengths$\Delta r/\lambda_D \simeq 1$. The particle weigh was set so at least 20 particles are loaded in each cell. For the OML simulations the grid is non-uniform as Fig. 8(b) shows. Near the probe the cells are set to $\Delta r/\lambda_D \simeq 0.1$ and progressively reach to $\Delta r/\lambda_D \simeq 1$ at the outer boundary. The computational domain is loaded uniformly with electrons and ions following the distribution (20). The particle weight is set to a value that results in at least 15 particles loaded the cells near the probe. The CIC weighting scheme is used for these computations. Electrons and ions are injected at each time-step from the boundaries of the domain. Particles that reach the boundaries of the domain or reach the probe are removed from the simulation. Zero electric field is set at the boundaries of the domain and a specified potential Φ_p is applied at the surface of the cylindrical probe. The electron current to the probe (retarded current) is considered as positive and the ion current (accelerated current) as negative, with the total current defined as $I_p = I_{ep} - I_{ip}$.

Simulations of Cases 1.1, 1.2, 2.1, 2.2 were conducted in order to analyze the influence of the ratio T_i/T_e on the currents collected by a stationary cylindrical probe operating in the finite probe ratio regime ($r_p/\lambda_D > 1$). The steady-state distribution of the potential is shown for $e\Phi_p/kT_e = 5, T_i/T_e = 1$ and $r_p/\lambda_D = 10$ in Fig. 9(a). The unsteady formation of the positively charged sheath around the probe is shown in Fig. 9(b). The comparisons shown in Figs. 9 and 10 show good agreement with results taken from Laframboise [42] and Peterson and Talbot [43]. Laframboise solved numerically the Vlasov–Poisson system (3)–(5) for a wide range of $T_i/T_e, -25 \leqslant e\Phi_p/kT_e \leqslant 25$ and $0 \leqslant r_p/\lambda_D \leqslant 100$. Laframboise' results are presented in graph-

Table 1
Input conditions for UPIC3dE simulations of cylindrical Langmuir probes.

Case #	1.1	1.2	2.1	2.2	3	4
R_D (m)	10^{-2}	10^{-2}	10^{-2}	5×10^{-3}	10^{-2}	5×10^{-2}
r_p	10^{-3}	10^{-3}	10^{-3}	5×10^{-4}	10^{-5}	5×10^{-3}
$n_e = n_i$ (m^{-3})	10^{16}	10^{16}	10^{16}	10^{16}	10^{16}	10^{16}
T_e (eV)	2	2	2	2	2	2
T_i/T_e	1	0.1	1	1	1	1
r_p/λ_D	10	10	10	5	0.1	50
$e\Phi_p/kT_e$	−10 to +10	−10 to +10	+2 to +9	+2 to +9	+1 to +9	−2
S_i	0	0	0	0	0	1 to 7

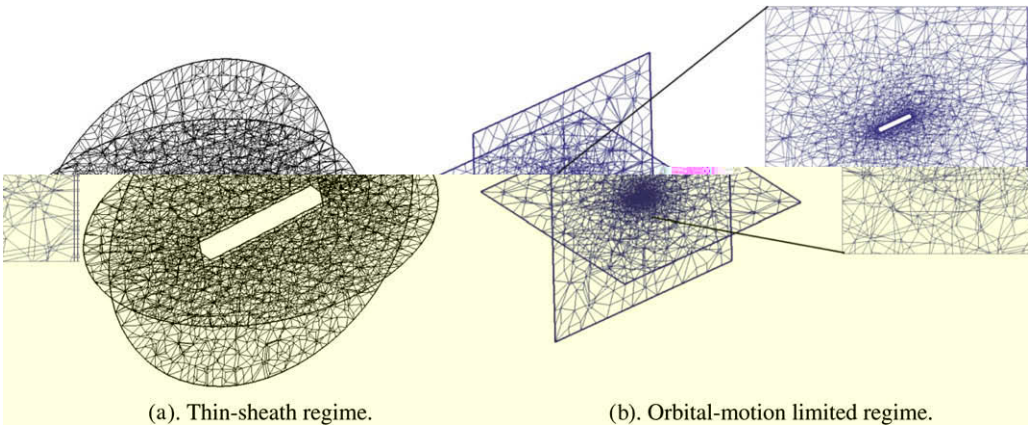

Fig. 8. Computational domains used in UPIC3dE simulations of Langmuir probes in stationary plasmas. The thin-sheath regime ($r_p/\lambda_D \gg 1$) and orbital-motion ($r_p/\lambda_D \ll 1$) limited regimes require vastly different grid configurations.

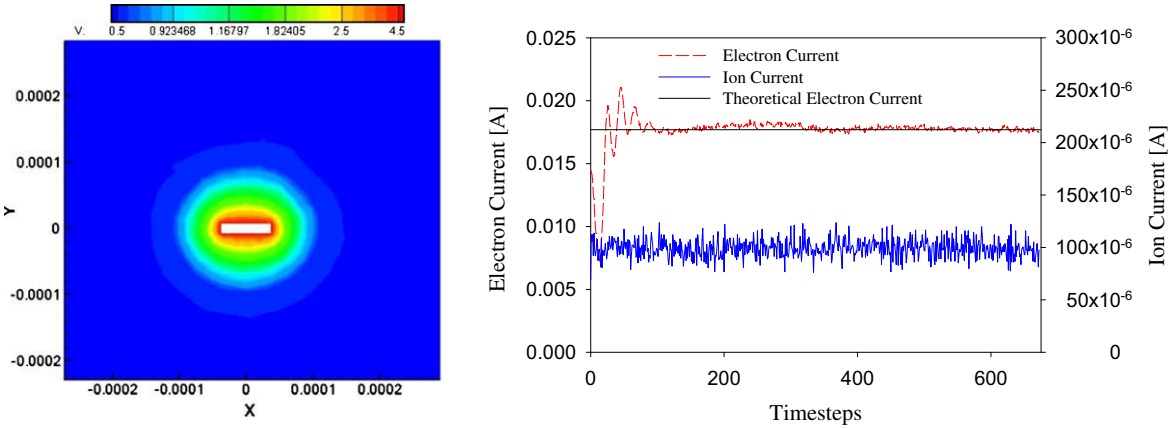

(a). Steady state potential distribution. (b). Electron and ion current.

Fig. 9. Potential and current from UPIC3dE simulation of a cylindrical Langmuir probe with $r_p/\lambda_D = 10$ and (case 1.1).

ical and tabular form and have been used widely in the literature. Petersen and Talbot developed regression expressions of Laframboise' results for probes with $5 \leqslant r_p/\lambda_D \leqslant 100$ at non-dimensional potential $\chi_p = e(\Phi_p - \Phi_s)/kT_e > 3$ and $T_i/Z_iT_e \leqslant 1$.

Simulation results from a stationary cylindrical probe operating in the near OML regime with $r_p/\lambda_D = 0.1, T_i/T_e = 1$ are presented in Fig. 11. The time evolution of the electron current collected by the probe at $e\Phi_p/kT_e = 5$ is shown in Fig. 11(a). The non-dimensional electron current is presented in Fig. 11(b) as a function of the non-dimensional potential for $1 \leqslant e\Phi_p/kT_e \leqslant 10$. The sheath formation leads to the fluctuations in the collected electron current before it reaches a steady state. The UPIC3dE results are in good agreement with the numerical results by Laframboise [42] and estimates based on the analytical solution by Kanal [44]. For a stationary probe in the OML regime and $V_p = |e|\Phi_p/kT_e > 0$ Kanal [44] provides the collected currents as

$$\begin{aligned} I_e &= en_e\sqrt{kT_e/2\pi m_e}(2\pi r_p L_p)\left(\frac{2}{\sqrt{\pi}}\sqrt{V_p} + e^{V_p}\mathrm{erfc}(\sqrt{V_p})\right), \\ I_i &= en_e\sqrt{kT_e/2\pi m_i}(2\pi r_p L_p)e^{-V_p}. \end{aligned} \tag{74}$$

Electron and ion currents collected by a cylindrical probe in the near thin-sheath regime ($r_p/\lambda_D = 50$) placed perpendicular to a flowing plasma with $T_i/T_e = 1$ are plotted in Fig. 12. The probe is biased at $e\Phi_p/kT_e = -2$ and currents are presented as a function of ion-speed ratio S_i. The UPIC3dE results are compared with estimates based on Kanal [44] who provides the electron current as

$$I_e = en_e\sqrt{kT_e/2\pi m_e}(2\pi r_p L_p)\exp(-e\Phi_p/kT_e). \tag{75}$$

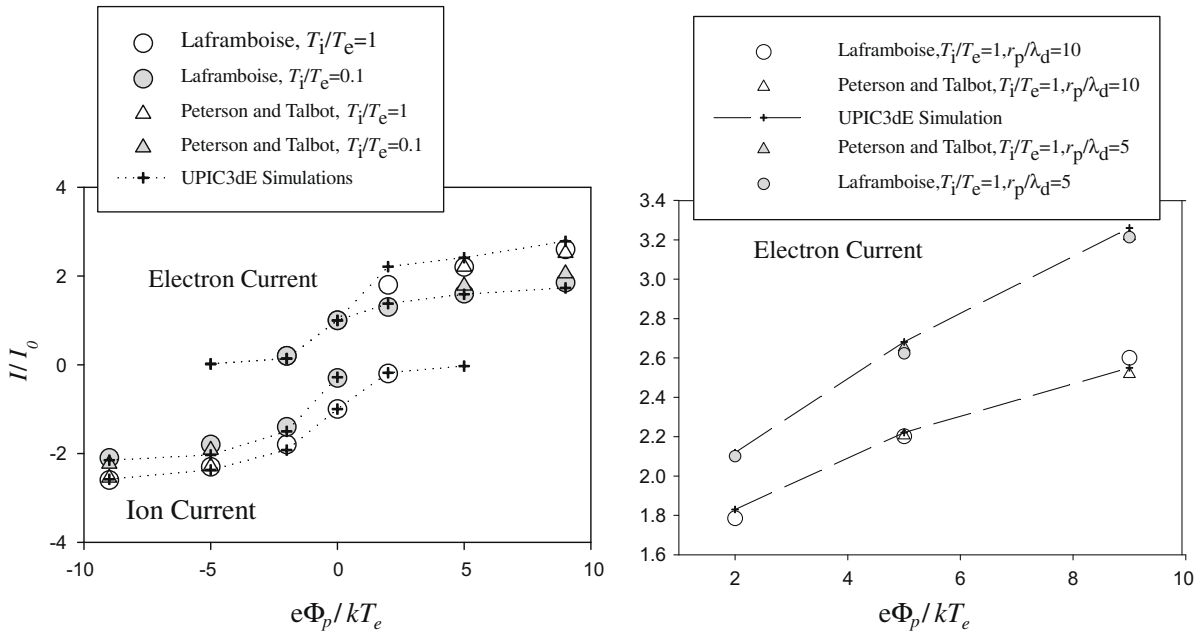

(a) Case 1.1 and 1.2

(b) Case 2.1 and 2.2

Fig. 10. UPIC3dE, analytical and previous computational results on current-voltage characteristics of a near thin-sheath cylindrical Langmuir probes in a stationary plasma.

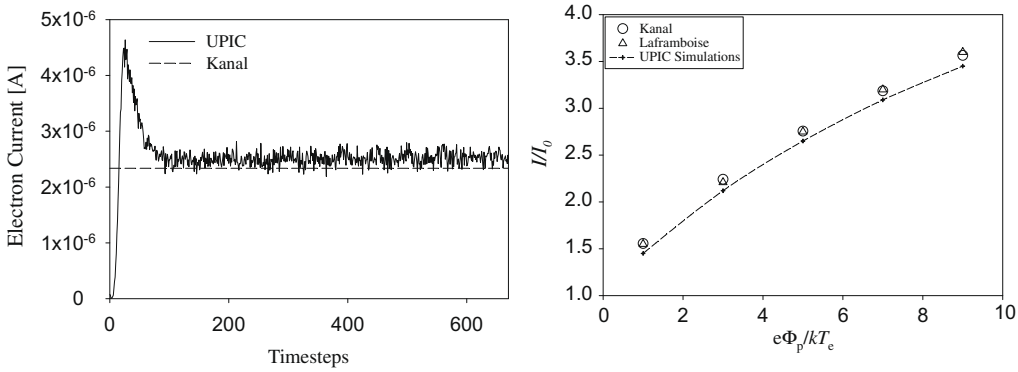

(a) Unsteady sheath formation for Case 3 and $e\Phi_p / kT_e = 5$.

Figure (b) Current-voltage for Case 3

Fig. 11. UPIC3dE and analytical results of currents collected by a cylindrical probe operating in the near-OML regime with.

The ion current to a perpendicular probe operating in the thin-sheath regime is given by Johnson and Murphree [45] as an asymptotic expression of Kanal's theory by

$$I_{\perp i} = (2\pi r_p L_p) e n_e \sqrt{\frac{kT_e}{2\pi m_i}} \frac{2}{\sqrt{\pi}} \exp(-S_i^2) \sum_{n=0}^{\infty} \left[\frac{S_i}{n!}\right]^2 \Gamma\left(n+\frac{3}{2}\right). \tag{76}$$

Fig. 12 shows the UPIC3dE results to be in good agreement with the theoretical values. At high-speed ratios the theory over-predicts the ion current because it does not account for probe-wake and space-charge effects that are modeled self-consistently with the UPIC3dE simulations.

6. Application of UPIC3dE to the simulation of a plasma microsensor

The UPIC3dE code is used in the simulation of the flow in a novel plasma sensor that features complex geometrical and physical characteristics as shown in Fig. 13. The directional micro-retarding potential analyzer (DmRPA) is designed by Par-

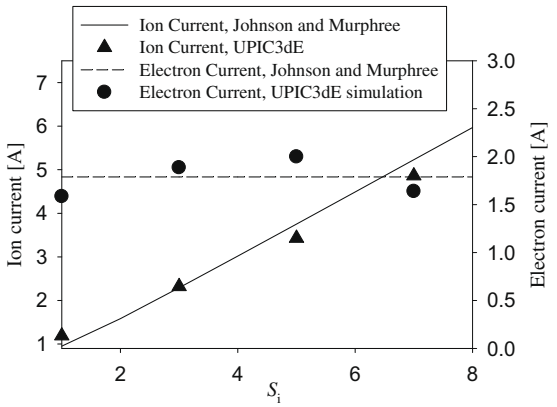

Fig. 12. UPIC3dE an analytical results for the electron and ion currents collected by a cylindrical Langmuir probe in a drifting plasma as a function of the ion-speed ratio.

tridge and Gatsonis [46] to operate in high-density flowing plasmas. The DmRPA consists of a floating electrode (FE), a negatively biased electron retarding electrode (ERE), two positively biased ion retarding electrodes (IRE) and a negatively biased secondary emission suppression electrode (SESE), as shown in Fig. 13. Unlike traditional RPAs the DmRPA has a large aspect ratio and includes a microgrid at its entrance that can further reduce the incoming flux. The energy distribution of ions in a plasma can be obtained by analyzing the DmRPA collector plate currents collected for different potential applied to the electrodes. A theory of current collection for the DmRPA has been developed by Partridge and Gatsonis [46] and extends the classic-RPA collection by accounting for flux reduction due to the microchannel walls and the microgrid. The DmRPA theory

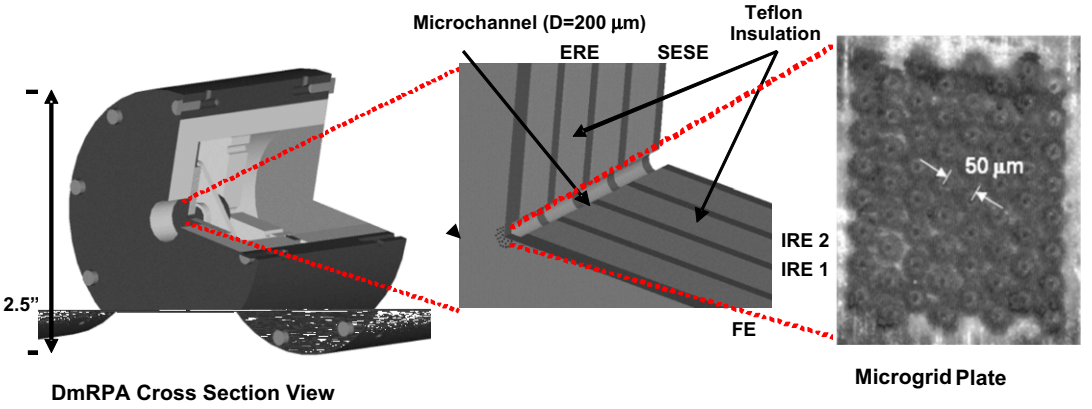

(a). The DmRPA with a detailed view of the microchannel and the microgrid with its holes.

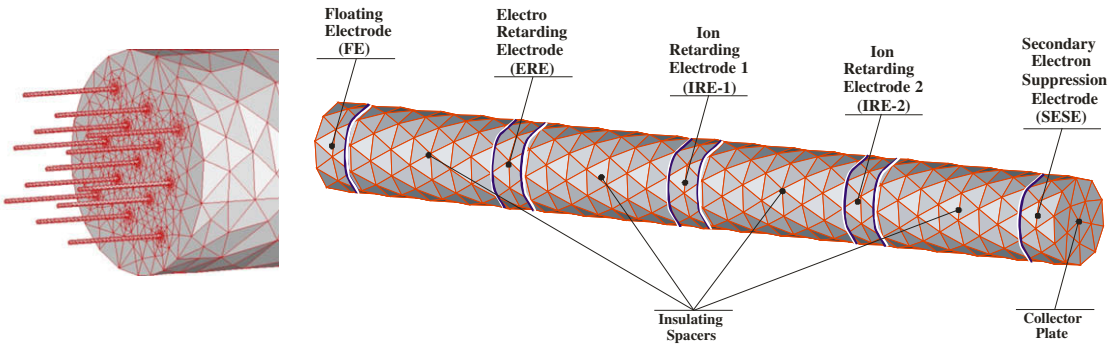

(b). Computational domain showing the microgrid holes and the microchannel used in the UPIC3dE simulations.

Fig. 13. DmRPA schematic showing the microgrid plate, microchannel, and electrodes. The computational domain used in the UPIC3E simulations.

Table 2
Input conditions for UPIC3dE simulations of the DmRPA without the microgrid plate (Case 1–6) and with the microgrid plate (Case 1a–6a).

Case #	1	1a	2	2a	3	3a	4	4a	5	5a	6	6a
$n_e = n_i$ (m^{-3})	10^{16}	10^{18}	10^{16}	10^{18}	10^{16}	10^{18}	10^{16}	10^{18}	10^{16}	10^{18}	10^{16}	10^{18}
$T_e = T_i$ (eV)	10	10	10	10	10	10	10	10	10	10	10	10
V_i (km/s)	15	15	15	15	15	15	15	15	15	15	15	15
Φ_{ERE}, Φ_{SESE} (V)	−50	−50	−50	−50	−50	−50	−50	−50	−50	−50	−50	−50
$\Phi_{IRE\text{-}1}$, $\Phi_{IRE\text{-}2}$ (V)	0	0	14.1	14.1	30	30	50	50	64.1	64.1	80	80

however, assumes equipotential surfaces inside the microchannel and neglects space-charge effects. The UPIC3de simulations of the DmRPA are used to explore such three-dimensional effects inside the microsensor. In cases where there is disagreement between theoretical predictions and simulations, UPIC3dE results can be used to construct the required *I–V* curves. In addition, UPIC3dE simulations elaborate the plasma flow inside the sensor and offer insights that can lead to optimization of its design.

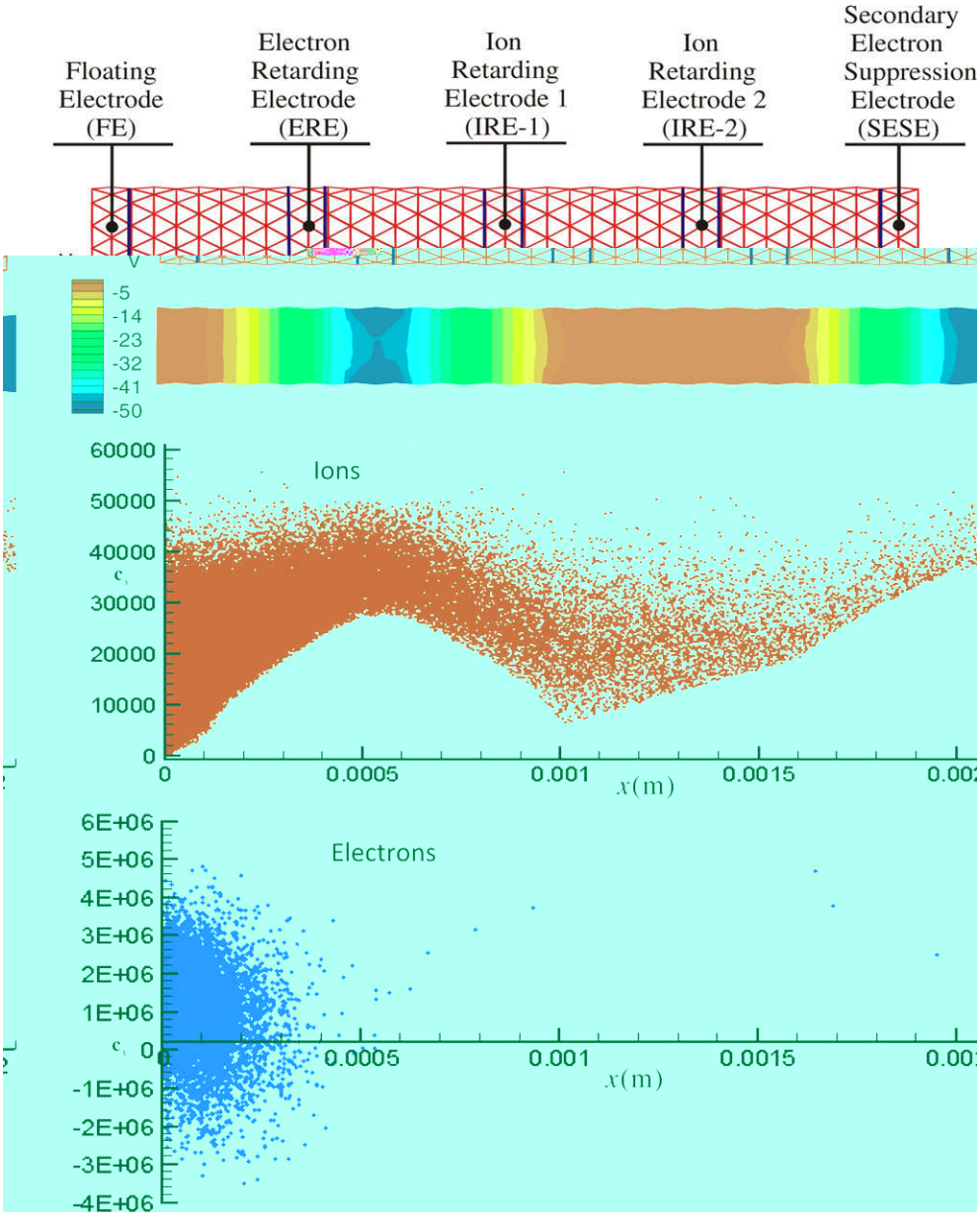

Fig. 14. UPIC3dE simulation of the DmRPA showing the simulation domain, the potential distribution and c_x vs. x phase-space plots for $\Phi_{ERE} = \Phi_{SESE} = -50$ V, $\Phi_{IRE\text{-}1} = \Phi_{IRE\text{-}2} = 0$ V (Case 1).

The first set of simulations (Cases 1–6) corresponds to the operation of the DmRPA without a microgrid attached at its entrance. A cylindrical computational domain representing the DmRPA microchannel is shown in Fig. 13. The domain length and radius are 2100 and 100 μm correspondingly. The domain is discretized with 3500 Delaunay cells that scale with the Debye length. Cells are loaded with at least 40 particles. The potential of the ERE and SESE electrodes is fixed at $\Phi_{ERE} = \Phi_{SESE} = -50$ V while the potential of the IRE-1 and IRE-2 electrodes is varied from 0 to 80 V. Neumann boundary condition is applied at all insulating surfaces. The plasma with parameters listed in Table 2 is injected from the left side of the domain with $n_e = n_i = 10^{16}$ m^{-3}, $T_e = T_i = 10$ eV, $V_e = V_i = 15,000$ m/s. Particles that reach any conductor (electrodes) or dielectric (teflon insulation) boundary are removed from the simulation.

The potential distribution inside of the domain and phase-plots for ions and electrons at the steady state are presented in Fig. 14 for case 1. The process of acceleration and deceleration of ions as they pass through the grids is evident in the phase plot of Fig. 14. The ion current that reaches the collector plate is evaluated in the simulations. Fig. 15 shows the dependence of the collector current on the ion retarding potential. Comparisons are made with the analytical expression of Partridge and Gatsonis [46]

$$I_i = \chi \frac{A q_i n_i}{2\pi^{3/2}} \left[\exp\left(-\beta_i^2 (\mathbf{c}_{eff} - \mathbf{V}_i)^2\right)/\beta_i + \mathbf{c}_{0i}\sqrt{\pi}\{1 - \mathrm{erf}(\beta_i(\mathbf{c}_{eff} - \mathbf{V}_i))\}\right]. \tag{77}$$

In the above equation, $\mathbf{c}_{eff}$ is the ion velocity corresponding to the effective retarding potential ϕ_{eff}, A is the DmRPA orifice area and χ_{RPA} is the transmission fraction defined as

$$\chi_{RPA} = N_{cc}(S_i, D)/N_{cc}(S_i, \infty). \tag{78}$$

In Eq. (78) S_i is the ion-speed ratio, D is the orifice diameter to length ratio and N_{cc} is defined as

$$N_{cc}(S_i, D) = \frac{n_i}{2\sqrt{\pi}\beta}\pi r^2 \{\left[\exp(-S_i^2) + S_i\sqrt{\pi}(1 + \mathrm{erf}(S_i))\right] - \left[\frac{2}{D^2}(\sqrt{1+D^2} - 1)\right] - -\frac{4S_i}{\sqrt{\pi}}\left[\frac{1}{D}\int_0^1 dY \int_0^{\tan^{-1}(D\sqrt{1-Y^2})} (1 + \mathrm{erf}(S_i \cos\phi))\cos\phi \exp(-S_i^2 \sin^2\phi) d\phi\right], \tag{79}$$

where r is the orifice radius, ϕ and Y are the geometrical integration parameters. Fig. 15(a) shows that the theoretical current follows the numerical results with differences at low and high applied potentials. The theory assumes an equipotential structure and no space-charge effects inside the microchannel. The UPIC3dE simulations show clearly that both effects are present.

The second set of simulations (Cases 1a–6a) corresponds to a more complex geometrical configuration of the DmRPA shown in Fig. 13 [46]. This configuration involves a microgrid plate of low transparency that is attached in front of the floating electrode. The microgrid is manufactured using a 100 μm thick molybdenum plate with 3 μm diameter holes. The hole-to-hole spacing is 50 μm with 30° offset as shown in Fig. 13. The microgrid with its holes is represented in the UPIC3dE simulations by an array of microcylinders attached to the floating electrode and the microchannel as shown in Fig. 13. The diameter and length of each microcylinder is 3 and 100 μm, respectively. Computational particles with the parameters listed in Table 2 are injected into the domain through the microcylinders.

The ion current measured at the collector plate surface is presented in Fig. 15(b) for various ion retarding potentials. Comparison is made with the estimates based on the analytical expression (77). Due to the low transparency of the microgrid, χ

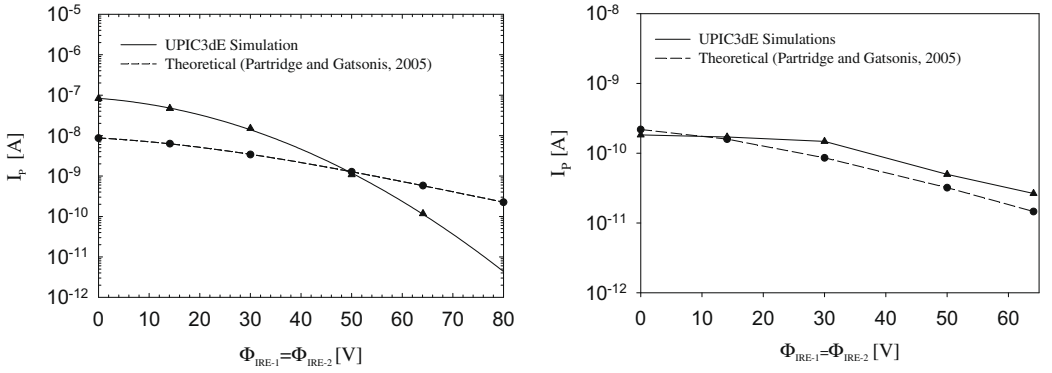

(a) DmRPA without a microgrid plate (case 1-6).

(b) DmRPA with a microgrid plate (case 1a-6a).

Fig. 15. UPIC3dE simulation of the DmRPA showing the collector plate current as a function of the ion retarding potential. Comparisons with theoretical estimates.

in Eq. (78) is taken to be a transmission fraction of the microgrid. In essence, the microgrid screens out the incoming ions and any further reduction in the flux occurs due to the retarding potentials but not the geometry. Differences are attributed to 3d effects, such as potential variation in the microcylinders and microchannel, not accounted for in the theoretical model.

7. Conclusions

We developed the mathematical formulation and computational implementation of a novel three-dimensional electrostatic particle-in-cell methodology on unstructured Delaunay–Voronoi tetrahedral grids (UPIC3dE). The method allows simulation of plasmas modeled by the Vlasov–Poisson system of equations in complex domains. The UPIC3dE method incorporates the duality of the Delaunay–Voronoi duality in all aspects of the particle-in-cell cycle. Charge assignment and field interpolation schemes of zero- and first-order are formulated for 3d unstructured tetrahedral grids based on the Hockney's theory of long-range constraints. The solution to Gauss's integral law is based on a finite-volume formulation that takes advantage of the Voronoi–Delaunay dual. Boundary conditions that include floating conductors are developed in 3d following Gauss's law. Algorithms for injection from boundaries, particle loading, and particle motion are developed for unstructured Delaunay grids. An efficient particle tracking algorithm is developed and allows the location of the particle and aids in the numerical integration of the equations of motion. Macroscopic multi-fluid and single-fluid plasma variables are obtained on nodes using the Voronoi dual.

Error and sensitivity analysis of the UPIC3dE method was performed. The effects of weighting scheme, particles/cell, grid scaling, and time-step on the numerical heating, slowing-down time, and deflection times were evaluated in a parametric investigation. A linear growth of the slowing-down time was found with increasing number of computational particles per cell. The magnitude of the slowing-down time is shown not to have any significant dependence on the order of the weighting scheme used. Overall, the linear weighting provides better results in these unstructured Delaunay computations, is easy to implement and is only slighter slower than zero-order. Higher order weighting/interpolation schemes should be able to further increase the heating time. However, construction of such schemes on 3d unstructured grids could lead to more complex analytical formulations that will increase the computational time.

The UPIC3dE numerical methodology and simulation code was validated by application to the problem of current collection by cylindrical Langmuir probes in stationary and moving collisionless plasmas. Numerical results are compared favorably with previous numerical and analytical solutions for a wide range of probe radius to Debye length ratios, probe potentials, and electron to ion temperature ratios.

The UPIC3dE code was applied to the simulation of the directional micro-retarding potential analyzer (DmRPA), a plasma microsensor that features complex geometrical and physical attributes. The DmRPA includes a microgrid plate that screens the flowing plasma before it enters a long microchannel embedded with a series of segmented electrodes. The current at the collector plate is compared favorably with theoretical predictions. The simulations show the complex structure of the potential inside the segmented microchannel, the phase-space of plasma species and the space-charge effects not captured by the theory.

Acknowledgment

This work was partially funded by AFOSR's Computational Mathematics Program under Grants F49620-00-1-0278, F49620-03-1-0219, and FA9550-06-1-0236.

References

[1] C.K. Birdsall, A.B. Langdon, Plasma Physics via Computer Simulations, Plasma Physics Series, 1991.
[2] R.W. Hockney, J.W. Eastwood, Computer Simulations Using Particles, IOP Publishing, 1999.
[3] J.P. Verboncoeur, Particle simulation of plasmas: review and advances, Plasma Physics and Controlled Fusion 47, Special issue 5A (2005) A231–A260.
[4] R.D. Ferraro, P.C. Liewer, V.K. Decyk, Dynamic load balancing for a 2D concurrent plasma PIC code, Journal of Computational Physics 109 (2) (1993) 329–341.
[5] J. Qiang, R.D. Ryne, S. Habib, V. Decyk, An object-oriented parallel particle-in-cell code for beam dynamics simulation in linear accelerators, Journal of Computational Physics 163 (2) (2000) 434–451.
[6] F. Wolfheimer, E. Gjonaj, T. Weiland, A parallel 3D particle-in-cell code with dynamic load balancing, Nuclear Instruments and Methods in Physics Research Section A: Accelerators, Spectrometers, Detectors and Associated Equipment 558 (1) (2006) 202–204.
[7] J.D. Blahovec, L.A. Bowers, J.W. Luginsland, G.E. Sasser, J.J. Watrous, 3-D ICEPIC simulations of the relativistic klystron oscillator, IEEE Transactions on Plasma Science 28 (3) (2000) 821–829.
[8] G.B. Jacobs, J.S. Hesthaven, High-order nodal discontinuous Galerkin particle-in-cell method on unstructured grids, Journal of Computational Physics 214 (1) (2006) 96–121.
[9] E. Sonnendrücker, J.J. Ambrosiano, S.T. Brandon, A finite element formulation of the Darwin PIC model for use on unstructured grids, Journal of Computational Physics 121 (2) (1995) 281–329.
[10] J. Wang, P. Liewer, V. Decyk, 3D electromagnetic plasma particle simulations on a MIMD parallel computer, Computer Physics Communications 87 (1–2) (1995) 35–53.
[11] J. Wang, D. Kondrashov, P.C. Liewer, S.R. Karmesi, Three-dimensional deformable-grid electromagnetic particle-in-cell for parallel computers, Journal of Plasma Physics 61 (3) (1999) 367–389.
[12] J. Villasenor, O. Buneman, Rigorous charge conservation for local electromagnetic field solvers, Computer Physics Communications 69 (2–3) (1992) 306–316.
[13] J.-S. Wu, K.-H. Hsu, F.-L. Li, C.-T. Hung, S.-Y. Jou, Development of a parallelized 3D electrostatic PIC-FEM code and its applications, Computer Physics Communications 177 (1–2) (2007) 98–101.

[14] J.J. Petillo, E.M. Nelson, J.F. DeFord, N.J. Dionne, B. Levush, Recent developments to the MICHELLE 2-D/3-D electron gun and collector modeling code, IEEE Transactions on Electron Devices 52 (5) (2005) 742–748.
[15] A. Spirkin, N.A. Gatsonis, Unstructured 3D PIC simulations of the flow in a retarding potential analyzer, Computer Physics Communications 164 (2004) 383–389.
[16] F. Hermeline, A finite volume method for solving Maxwell equations in inhomogeneous media on arbitrary meshes, Comptes Rendus Mathematique 339 (12) (2004) 893–898.
[17] V. Vahedi, G. DiPeso, Simultaneous potential and circuit solution for two-dimensional bounded plasma simulation codes, Journal of Computational Physics 131 (1) (1997) 149–163.
[18] R.D. Löhner, J. Ambrosiano, A vectorized particle tracer for unstructured grids, Journal of Computational Physics 91 (1) (1990) 22–31.
[19] R.W. Hockney, Measurements of Collision and Heating Times in a Two-Dimensional Thermal Computer Plasma, Journal of Computational Physics 8 (1971) 19–44.
[20] D.C. Montgomery, D.A. Tidman, Plasma Kinetic Theory, McGraw-Hill, 1964.
[21] S. Ichimaru, Basic Principles of Plasma Physics: A Statistical Approach, Westview Press, 1994.
[22] J.M. Burgers, Flow Equations for Composite Gases, Academic Press, New York, 1969.
[23] S.I. Braginksi, Transport properties in a plasma, in: M.A. Leontovich (Ed.), Review of Plasma Physics, Consultants Bureau, New York, 1965.
[24] J. A Bittencourt, Fundamental of Plasma Physics, Pergamon Press, 1986.
[25] M. Mitchner, C.H. Kruger, Partially Ionized Gases, Wiley Series in Plasma Physics, 1992.
[26] K. Kovalev, Development of a 2D/3D Unstructured Adaptive Grid Generator for Direct Simulation Monte Carlo Computations, M.S. Thesis, WPI, Worcester, MA, July 2000.
[27] D.F. Watson, Computing the *N*-dimensional delaunay tessellation with application to Voronoi prototypes, The Computer Journal 24 (2) (1981) 167–172.
[28] H. Borouchaki, P.L. George, Aspects of 2-d Delaunay mesh generation, International Journal for Numerical Methods in Engineering 40 (11) (1997) 1957–1975.
[29] G.A. Bird, Molecular Gas Dynamics and the Direct Simulation of Gas Flows, Clarendon Press, Oxford, 1994.
[30] H.C. Kim, Y. Feng, J.P. Verboncoeur, Algorithms for accurate collection, ejection, and loading in particle simulations, Journal of Computational Physics 223 (2) (2007) 629–642.
[31] H.C. Kim, Y. Feng, J.P. Verboncoeur, Algorithms for accurate collection, ejection, and loading in particle simulations, Journal of Computational Physics 223 (2) (2007) 629–642.
[32] Y. Saad, Iterative Methods for Sparse Linear Systems, SIAM, 2003.
[33] J.P. Verboncoeur, M.V. Alves, V. Vahedi, C.K. Birdsall, Simultaneous potential and circuit solution for 1D bounded plasma particle simmulation codes, Journal of Computational Physics 104 (1993) 321.
[34] K.F. Riley, M.P. Hobson, S. Bence, Mathematical Methods for Physics and Engineering: A Comprehensive Guide, Cambridge University Press, 2002.
[35] O. Buneman, Time-reversible difference procedures, Journal of Computational Physics 1 (4) (1967) 517–535.
[36] J.P. Boris, Relativistic Plasma Simulation-Optimization of a Hybrid Code, Proceedings of the Fourth Conference on Numerical Simulation of Plasma, Naval Res. Lab, Washington DC, 2–3 November, 1970, pp. 3–67.
[37] C. Hirsch, Numerical Computation of Internal and External Flows, vol. 1, John Wiley, Berlin, 1988.
[38] C.K. Birdsall, N. Maron, Plasma self-heating and saturation due to numerical instabilities, Journal of Computational Physics 36 (1980) 1–19.
[39] H. Ueda, Y. Omura, H. Matsumoto, T. Okuzawa, A study of the numerical heating in electrostatic particle simulations, Computer Physics Communications 79 (1994) 249–259.
[40] P.J. Mardahl, PIC Code Charge Conservation, Numerical Heating, and Parallelization; Application of XOOPIC to Laser Amplification via Raman Backscatter, Ph.D. Dissertation, University of California, Berkeley, 2001.
[41] B.A. Trubnikov, Particle Interactions in a Fully Ionized Plasma, Reviews of Plasma Physics, Consultants Bureau, 1965.
[42] J.G. Laframboise, Theory of Spherical and Cylindrical Langmuir Probes in a Collisionless, Maxwellian Plasma at Rest, Univ. Toronto Institute of Aerospace Studies, Report No. 100, June, 1966.
[43] E.W. Peterson, L. Talbot, Collisionless electrostatic single-probe and double-probe measurements, AIAA Journal 8 (12) (1970).
[44] M. Kanal, Theory of current collection of moving cylindrical probes, Journal of Applied Physics 35 (6) (1964).
[45] B.H. Johnson, D.L. Murphree, Plasma velocity determination by electrostatic probes, AIAA Journal 7 (10) (1969) 2028–2030.
[46] J. Partridge, N.A. Gatsonis, Characterization of high-density flowing plasmas using a directional micro-retarding potential analyzer, in: IEPC-2005-170, 29th International Electric Propulsion Conference, Princeton, NJ, November 2005.